Surface & Coatings Technology 437 (2022) 128275

Contents lists available at ScienceDirect

Surface & Coatings Technology

journal homepage: www.elsevier.com/locate/surfcoat

Pathway to tailor the phase composition, microstructure and mechanical properties of pulsed laser deposited cobalt-substituted calcium phosphate coatings on titanium

Smilja Marković [a,*], Julietta V. Rau [b,c], Angela De Bonis [d], Giovanni De Bellis [e,f], Zoran Stojanović [a], Ljiljana Veselinović [a], Miodrag Mitrić [g], Nenad Ignjatović [a], Srečo Davor Škapin [h], Damjan Vengust [h]

[a] Institute of Technical Sciences of SASA, Kneza Mihaila 35/IV, Belgrade, Serbia
[b] Istituto di Struttura della Materia, Consiglio Nazionale delle Ricerche (ISM-CNR), Via del Fosso del Cavaliere 100, Rome 00133, Italy
[c] I.M. Sechenov First Moscow State Medical University, Institute of Pharmacy, Department of Analytical, Physical and Colloid Chemistry, Trubetskaya 8, build. 2, Moscow 119991, Russian Federation
[d] Dipartimento di Scienze, Università della Basilicata, Via dell'Ateneo Lucano 10, Potenza 85100, Italy
[e] DIAEE-Department of Astronautical, Electrical and Energy Engineering, via Eudossiana 18, Rome 00184, Italy
[f] CNIS-Research Center on Nanotechnology Applied to Engineering, P.le Aldo Moro 5, Rome 00185, Italy
[g] Vinča Institute of Nuclear Sciences, University of Belgrade, Mike Alasa, Belgrade, Serbia
[h] Jožef Stefan Institute, Jamova cesta 39, 1000 Ljubljana, Slovenia

ARTICLE INFO

Keywords:
Coatings
Cobalt-substituted hydroxyapatite
Calcium phosphate
Pulsed laser deposition

ABSTRACT

Dense calcium phosphate-based ceramics were fabricated to be used as targets for pulsed laser deposition (PLD). Nanostructured cobalt-substituted hydroxyapatite (Co:HAP) was used as a starting powder. To vary phase composition and microstructure of targets, two sintering approaches were applied, conventional (CS) and two-step sintering (TSS). The obtained results show that in both cases biphasic calcium phosphate (BCP) ceramics (targets) were prepared, with slightly different HAP-to-β–TCP amount ratio and a significantly different microstructure. While the CS method yielded fully dense ceramics with an average grain size of 1.3 μm, the ceramics prepared by TSS had a density of 98.5%, with a predominant grain size below 100 nm. (Ca + Co)P coatings were prepared by PLD of (Ca + Co)P targets. The temperature of the Ti substrate was adjusted to be 25 and 500 °C. The results show that the phase composition of (Ca + Co)P coatings depended on the phase composition of targets as well as on the temperature of the Ti substrate. The coating prepared at 25 °C using CS target consisted of three calcium phosphate phases, HAP, β–TCP and α–TCP; when the TSS target was used, the coating was biphasic, containing HAP and β–TCP. When the substrate was heated to 500 °C, regardless of whether the CS or the TSS target was used, the deposited coatings were composed of HAP and α–TCP. Due to different phase compositions, the (Ca + Co)P coatings deposited at 25 °C showed an improved hardness compared to those deposited at 500 °C. The obtained results confirmed that the phase composition, morphology and mechanical properties of 0.3 μm thick (Ca + Co)P coatings on a Ti substrate can be tailored by employing (Ca + Co)P targets with different microstructures, and also by varying the temperature of the Ti substrate during deposition experiments.

1. Introduction

Calcium phosphate (CaP) materials have been in clinical use since the 1980s [1]. Calcium phosphates include: amorphous calcium phosphate (ACP), dicalcium phosphate dihydrate (DCPD, $CaHPO_4 \times 2H_2O$), octacalcium phosphate (OCP, $Ca_4H(PO_4)_3 \times 2.5H_2O$), hydroxyapatite (HAP, $Ca_{10}(PO_4)_6(OH)_2$), tricalcium phosphate (TCP, $Ca_3(PO_4)_2$) as well as combinations of two or more calcium phosphates [2]. The most important properties of CaP biomaterials, bioactivity and the rate of biodegradation, are determined by the chemical composition of the material [3–6]. The most stable calcium phosphate phase, with a very slow bioresorption rate, is HAP, while β-TCP is a bioresorbable material

* Corresponding author.
E-mail address: smilja.markovic@itn.sanu.ac.rs (S. Marković).

https://doi.org/10.1016/j.surfcoat.2022.128275
Received 20 January 2022; Received in revised form 18 February 2022; Accepted 21 February 2022
Available online 28 February 2022

which dissolves faster than HAP in a biological environment [6]. HAP can be used when long-term stability is necessary; nevertheless, the presence of β-TCP could be beneficial due to a better protein adsorption capacity than pure HAP [6]. Thus, the biodegradation rate and bioactivity can be controlled by tailoring the HAP-to-β-TCP ratio.

As especially important application of CaPs is in the use in coatings [7]. In clinical practice, in the field of regenerative medicine, calcium phosphate coatings are widely used to improve the biocompatibility and stability of metallic (Ti), alloy (based on Ti, Co, Cr, Mo and Ni) or stainless steel implants, as well as to prevent tissue irritation or inflammation associated with corrosion [3,8,9]. Contrariwise, biocompatible CaP coatings promote osteointegration and osteoconductivity, enhance the growth of osteoblast cells and their proliferation, etc. [3,8].

It has been recently shown that substituted HAP coatings can have additional properties, compared to conventional CaP coatings, e.g. osteoinduction or antibiotic activity [10]. Especially important is substitution with essential cations, such as cobalt (II), sodium, and manganese (II). Even though a significant number of studies deal with Co-doped HAP, in the form of powder or bulk, showing (1) antimicrobial activity against *S. aureus*, *Micrococus luteus*, and *Shigella flexneri* [11], (2) an angiogenic effect of Co^{2+}, which could favor the neovascularization of newly formed bone tissue by inducing hypoxia, or (3) the stimulation of the osteogenesis inside a mandibular defect, 6 months after implantation [12], the number of paper about Co:HAP coatings is negligible [13].

Continuing our previous studies on the fabrication of hydroxyapatite-based nanoparticles [14], and dense nanostructured ceramics [6], in the present study, we deal with coatings based on them. The main idea of this study has been to develop a model system for engineering of nanostructured calcium phosphate-based coatings on a titanium substrate using sintered CaP-based pellets as targets for PLD. An important processing goal has been (1) to prepare sintered CaP-based pellets with a high density and a uniform grain-size distribution, then (2) to establish a correlation between the phase composition (HAP-to-β-TCP ratio) and microstructure (average grain size and density) of targets and the phase composition, morphology and mechanical properties (hardness and Young's modulus) of the prepared coatings. In this study, nanostructured hydroxyapatite powder doped with 5 at.% of cobalt (II) ions was used as a starting material. To vary the phase composition and microstructure of the sintered pellets, which were further used as targets for PLD, two sintering approaches were applied, conventional (CS) and two-step sintering (TSS) method.

2. Experimental part

2.1. Preparation and characterization of Co:HAP starting powder

Based on our previous investigations [12,15–18], especially those showing that Co:HAP with 5 at.% of Co optimally influenced osteoporotic alveolar bone regeneration in Wistar rats, when after 24 weeks of reconstruction bone defects were completely filled with the new bone [12,17], stoichiometric hydroxyapatite with 5 at.% of Co^{2+} substituted for Ca^{2+} was chosen for the preparation of targets for PLD. Further in the text, the starting powder is abbreviated as Co:HAP.

The Co:HAP powder was prepared by the hydrothermal processing of the precipitate using the procedure described in detail in our previous paper [15]. The ratio of (Ca + Co)/P was adjusted to be 1.67.

A qualitative and quantitative elemental analysis of the Co:HAP powder was completed on an inductively coupled plasma (ICP) spectrometer (iCAP Thermo Scientific 6300). Before the analysis, the sample was diluted in concentrated HCl. The results obtained by ICP were used for the calculation of the stoichiometric formulae. The phase composition of the Co:HAP powder was determined employing an X-ray diffraction analysis (XRD). The XRD data were collected on a Rigaku Ultima IV diffractometer in Bragg–Brentano geometry, with Ni-filtered Cu $K_{\alpha 1,2}$ radiation (λ = 1.54178 Å); the working conditions were 40 kV and 20 mA. The diffraction intensity was measured from 10 to 70° 2θ, with a step size of 0.02 and an acquisition rate of 2° per min. The crystal phases were identified by comparing the collected data with those reported in the *Inorganic Crystal Structure Database* (*ICSD*). The unit cell parameters were calculated using the least-squares method by the LSUCRI computing program while the crystallite sizes were calculated from XRD line-broadening using the Scherrer equation [19]. Room-temperature μ-Raman spectra were recorded with a NT-MDT NTEGRA Spectra I system equipped with an optical microscope and a EMCCD detector. A helium neon laser operating at a probing wavelength of 633 nm with the power of 2.5 mW was used for excitation. The spectra were recorded in the wavenumber interval of 60–1800 cm^{-1} with a resolution of 4 cm^{-1}. The raw data were smoothed using Savitzky-Golay smoothing filter. The baseline was removed using the second order polynomials and subsequently spectra were normalized. Functional groups on the Co:HAP particles and possible residues of the reagents used during HT processing were inspected by Fourier transform infrared (FT-IR) spectroscopy. The spectra were recorded on a Thermo Scientific™ Nicolet™ iS™10 FT-IR Spectrometer equipped with an attenuated total reflectance (ATR) accessory. ATR/FT-IR measurements were done in the wavenumber interval of 400–4000 cm^{-1} with a resolution of 4 cm^{-1}. The oxidation state of cobalt ions were determined via magnetic measurements in the high temperature (i.e. paramagnetic) region 100 K < T < 300 K using a Quantum Design's SQUID-based magnetometer MPMS XL-5. The experimental data were fitted to the Curie-Weiss law. The morphology of the Co:HAP particles was observed by field emission scanning electron microscopy (FE-SEM, Ultra plus, Carl Zeiss, Germany). The particle size distribution in water suspensions was determined by a laser light-scattering particle size analyzer (PSA, Mastersizer 2000; Malvern Instruments Ltd., Malvern, Worcestershire, U.K.). The primary particle size, morphology and crystal structure were investigated by transmission electron microscopy (TEM), high-resolution transmission electron microscopy (HRTEM), and selective area of electron diffraction (SAED) (Jeol 2100, operating at 200 keV). The specific surface area (SSA) and the porosity of particles were determined based on a N_2 adsorption–desorption isotherm at −195.8 C using an ASAP 2020 (Micromeritics Instrument Corporation, Norcross, GA, USA). Prior to analysis, the samples were degassed under reduced pressure at 120 °C for 10 h. The thermal behavior and the phase stability of the Co:HAP powder were determined by simultaneous thermogravimetric/differential thermal analysis (TG/DTA; Setsys, SETARAM Instrumentation, Setaram, Cailure, France). The analysis was performed in the temperature range between 30 and 1200 °C under the air flow of 20 ml·min^{-1}, in an Al_2O_3 pan. The heating profile was set as follows: the material was stabilized at 30 °C for 5 min then heated to 1200 °C with the heating rate of 10°·min^{-1}.

2.2. Preparation and characterization of the CS and TSS targets

The targets for PLD experiments were prepared by sintering procedures. The synthesized Co:HAP powder was uniaxially pressed in ∅ 10 mm die under a pressure of 120 MPa; each of compacts has the thickness circa 5 mm. Green compacts with 50 ± 2% TD were prepared. The sintering of the green compacts was carried out in air atmosphere by (1) conventional (CS) and (2) two-step sintering (TSS) methods; in both cases the sintering were done in dilatometer (TMA, Setsys, SETARAM Instrumentation, Setaram, Cailure, France). The sintering conditions for CS and TSS were chosen due to both, thermal stability of the powder determined by simultaneous TG/DTA analysis and our previous experience on sintering of HAP nanopowders [6,14]. The conventional sintering was done by the heating rate of 10 °C·min^{-1} up to 1100 °C, with the dwell time of 1 h and the cooling rate of 10 °C·min^{-1}. TSS was performed in following conditions: the samples were heated by the rate of 5 °C·min^{-1} up to 950 °C and after holding for 5 min at 950 °C, the samples were cooled down by the rate of 50 °C·min^{-1} to 850 °C and subsequently kept in the second-step temperature for 12 h. After the

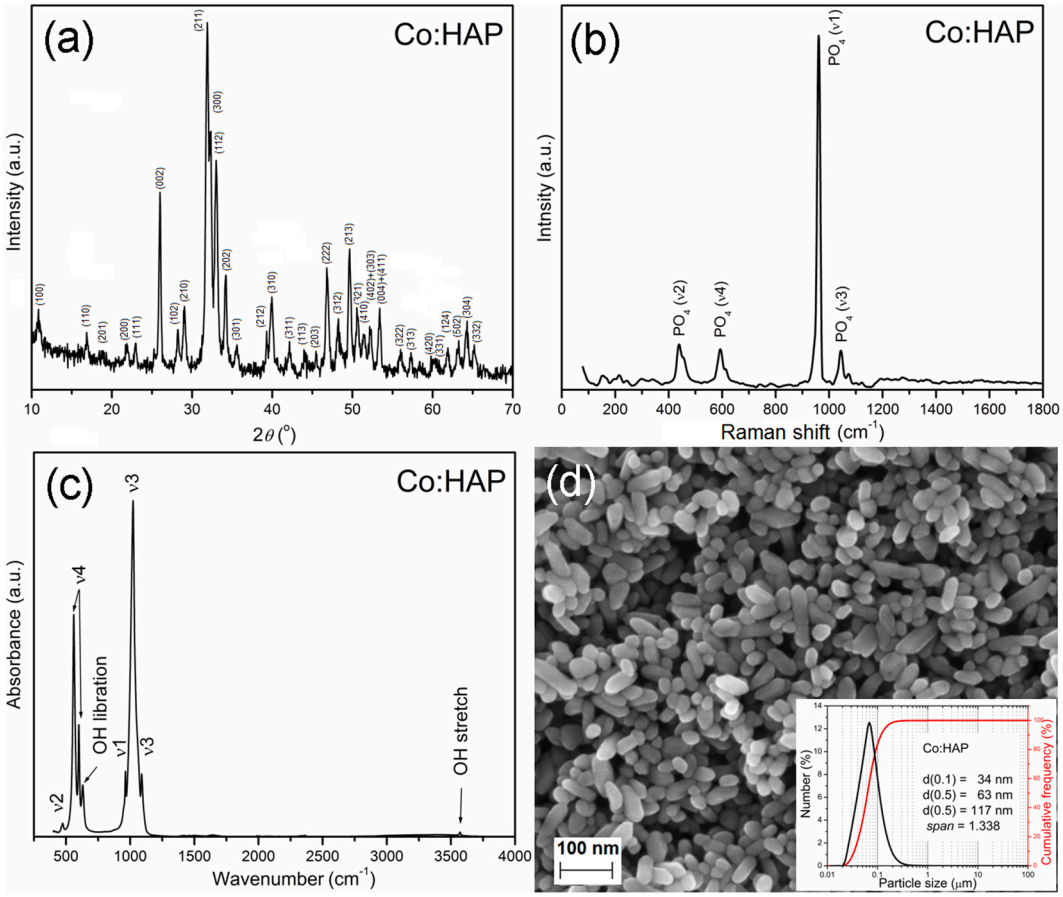

Fig. 1. (a) XRD pattern, (b) Raman spectrum, (c) FTIR spectrum, and (d) FESEM image with the inserted particle size distribution of the Co:HAP powder.

sintering procedure samples were cooled down to 30 °C with the rate of 5 °C·min^{-1}. The density of cylindrical samples, both pressed and sintered, was calculated from the weight to volume ratio.

Phase composition, crystal structure and functional groups were determined by XRD, Raman and FTIR spectroscopy; the measurements were done on powder after the pallets were crushed. FESEM characterization was done on polished, thermally etched and carbon coated pallets surface. All the measurements were done using the same equipment and experimental conditions as for starting Co:HAP powder.

2.3. Preparation and characterization of (Ca + Co)P coatings on Ti

The ablation and deposition experiments were carried out in a stainless steel vacuum chamber equipped with a rotating target holder and a heated substrate support. During the deposition process, the working pressure in the vacuum chamber was 1.5×10^{-4} Pa. The coatings were deposited on a Ti substrate for 2 h, with the distance between the target and the substrate fixed at 2.0 cm and substrate temperatures of 25 and 500 °C. The laser source was a frequency doubled ($\lambda = 532$ nm) Nd:YAG laser (Quanta System) with a pulse duration of 7 ns and a repetition rate of 10 Hz. The laser beam was incident at an angle of 45° on the target surface and focused by a 35 cm focus lens. The laser power was fixed at 270 mW and the spot on the target was of 7×10^{-4} cm^2.

The XRD and Raman measurements were done using the same equipment and in the same experimental conditions as for the powders. FTIR spectra were acquired by a Jasco 460Plus interferometer. For each sample 100 spectra were collected in the wavenumber region 400–4000 cm^{-1}, with a resolution of 4 cm^{-1}. The morphology of the deposited coatings was studied by scanning electron microscopy (SEM) and atomic force microscopy (AFM). SEM characterization was done on a Philips-FEI ESEM XL30 instrument, while AFM characterization was carried out on a Bruker Dimension Icon system, equipped with a Nanoscope *V* controller. The AFM micrographs were acquired in the tapping mode, using n-doped Si probes (Bruker RTESP300) with a resonant frequency of roughly 300 kHz, at a scan rate between 0.3 Hz and 1 Hz. At least three different 10 μm × 10 μm areas were scanned for each sample and the resulting roughness coefficients were given as average values. The hardness of the coatings was measured on a Leica VMHT microhardness apparatus (Leica GmbH, Germany) supplied with a standard Vickers pyramidal indenter (square-based diamond pyramid with a 136° face angle). The 8 loads ranging from 0.245 up to 19.61 N were applied for 15 s at the loading and unloading speed of 5×10^{-6} m/s. For each applied load, approximately 10 to 15 indentations were made. The hardness of the Ti substrate was measured in a separate experiment to be 1.8 ± 0.3 GPa. For the deposited coatings, the measured hardness corresponds to the coating-substrate composite system. In order to extract the intrinsic hardness of coatings from these experimental data, the Joensson and Hogmark approach was applied [20]. The applied procedure is described in detail in our previous works [9,21]. The SEM characterization of the films deposited on polished monocrystalline silicon substrates was done on a Philips-FEI ESEM XL30 (Hillsboro, Oregon, USA) instrument equipped with a tungsten filament and operating at 30 kV. Several images at magnifications ranging from 2000× to 20,000× were taken throughout the surface of the coatings to confirm the homogeneity of the films. The atomic force microscopy (AFM) characterization was done using a Bruker Dimension Icon system, equipped with a Nanoscope V controller. The AFM micrographs were acquired in the tapping mode, by using n-doped Si probes (Bruker RTESP300) with a resonant frequency of roughly 300 kHz, at a scan rate

Table 1
Phase composition, unit cell parameters, crystallites size and crystallinity of Co:HAP powder, TSS and CS sintered pellets, and coatings obtained by RF magnetron sputtering.

Sample			Phase composition	Unit cell parameters		Crystallites size, D (nm)	Crystallinity (%)
				$a = b$ (Å)	c (Å)		
Co:HAP powder			HAP	9.4170(3)	6.8671(2)	~26	76
Sintered targets	TSS		β-TCP (27.45%)	10.403(1)	37.357(9)	~90	81
			HAP (72.55%)	9.398(7)	6.898(7)	~55	
	CS		β-TCP (30.82%)	10.398(5)	37.416(1)	~80	84
			HAP (69.18%)	9.399(2)	6.901(5)	~60	
Coatings	TSS	RT	HAP β–TCP	/	/	/	61
		500 °C	HAP α–TCP	/	/	/	67
	CS	RT	HAP β–TCP α–TCP	/	/	/	62
		500 °C	HAP α–TCP	/	/	/	65

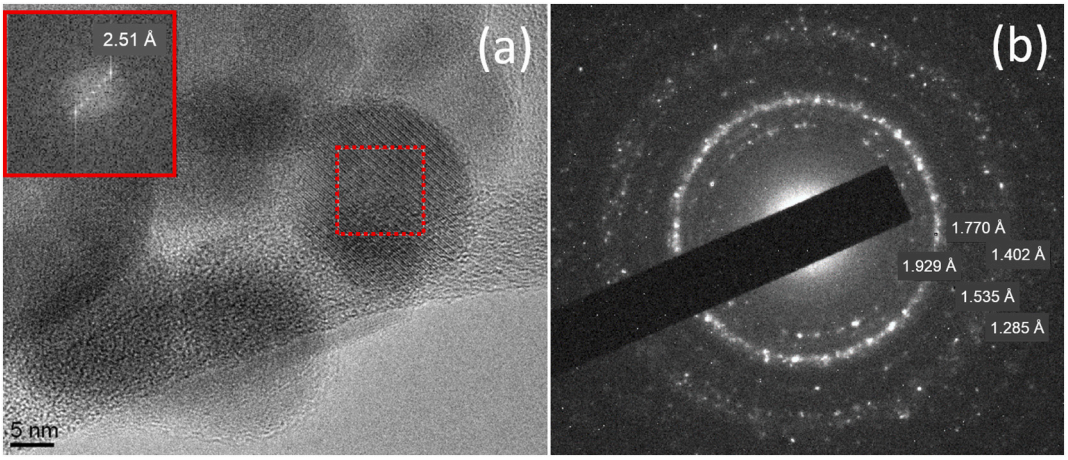

Fig. 2. (a) HRTEM with the inserted FFT, and (b) SAED of the Co:HAP powder.

between 0.3 Hz and 1 Hz. At least three different 10 μm × 10 μm areas were scanned for each sample and the resulting roughness coefficients were averaged.

3. Results and discussion

3.1. Characteristics of starting Co:HAP powder

A detailed characterization of the Co:HAP powder was presented in our previous papers [15,16]. Here, we point out the powders' properties, precisely: phase composition, stoichiometry, degree of crystallinity, morphology, particle size distribution, and specific surface area, which influenced the powder's stability and sinterability, finally determining the quality of targets for laser deposition.

XRD, Raman, and FTIR data (Fig. 1a–c) supported by the results of the ICP analysis show that the Co:HAP powder has a pure hydroxyapatite crystal structure, with a crystallinity degree of 76%, and with the stoichiometric formulae $Ca_{9.57}Co_{0.43}(PO_4)_6(OH)_2$ i.e. (Ca + Co)/P ratio of 1.67. The calculated values of unit cell parameters, crystallites size and the crystallinity of the Co:HAP powder are listed in Table 1. The morphology analysis accompanied with particle size distribution show that the Co:HAP powder has uniform, slightly elongated, particles with an average particle size of about 60 nm and without agglomeration, Fig. 1d.

Results of the magnetic measurements, successfully fitted to a Curie-Weiss law, yields the value of the effective magnetic moment per cobalt ion of 5.1 μ_B. This value, falling in the 4.3–5.3 μ_B range, confirms that in the Co:HAP powder cobalt ions are in +2 oxidation state in an octahedral environment [16]. The position of cobalt ions in the HAP crystal lattice is confirmed by FFT/SAED analyses via changes of the d values. The lattice fringe of 2.51 Å (FFT inset at HRTEM Fig. 2a) which

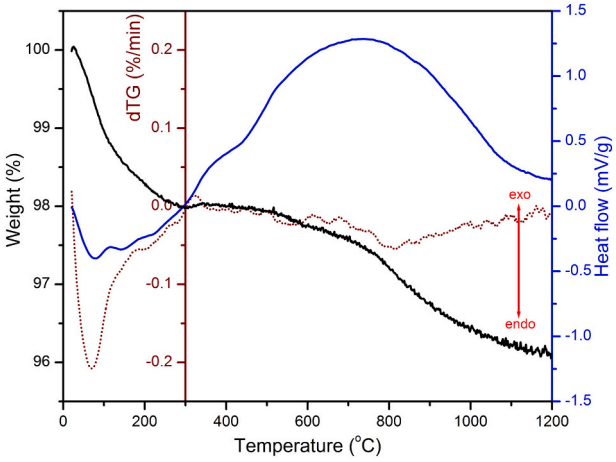

Fig. 3. TG/dTG/DTA plots of the Co:HAP powder.

corresponds to the lattice plane (301) is in agreement with the corresponding d value of 2.52 Å obtained from the XRD analysis (Fig. 1a); however, it is smaller than the value reported for pure HAP (2.529 Å, ICSD 89-6440). Similarly, all crystal lattice planes detected in diffraction rings at SAED (Fig. 2b) are slightly smaller than those reported at ICSD 89-6440. Even such small decreases of the d value of the Co:HAP crystal lattice compared to pure HAP confirms the incorporation of Co^{2+} ions with a smaller ionic radius (0.070 nm) in the place of Ca^{2+} ions (0.099 nm) in the HAP crystal structure.

The BET analysis of the Co:HAP powder shows the SSA value of 35.7 m^2/g, with V_{total} of 0.2153 cm^3/g, V_{meso} 0.2125 cm^3/g and D_{av} 23.3 nm.

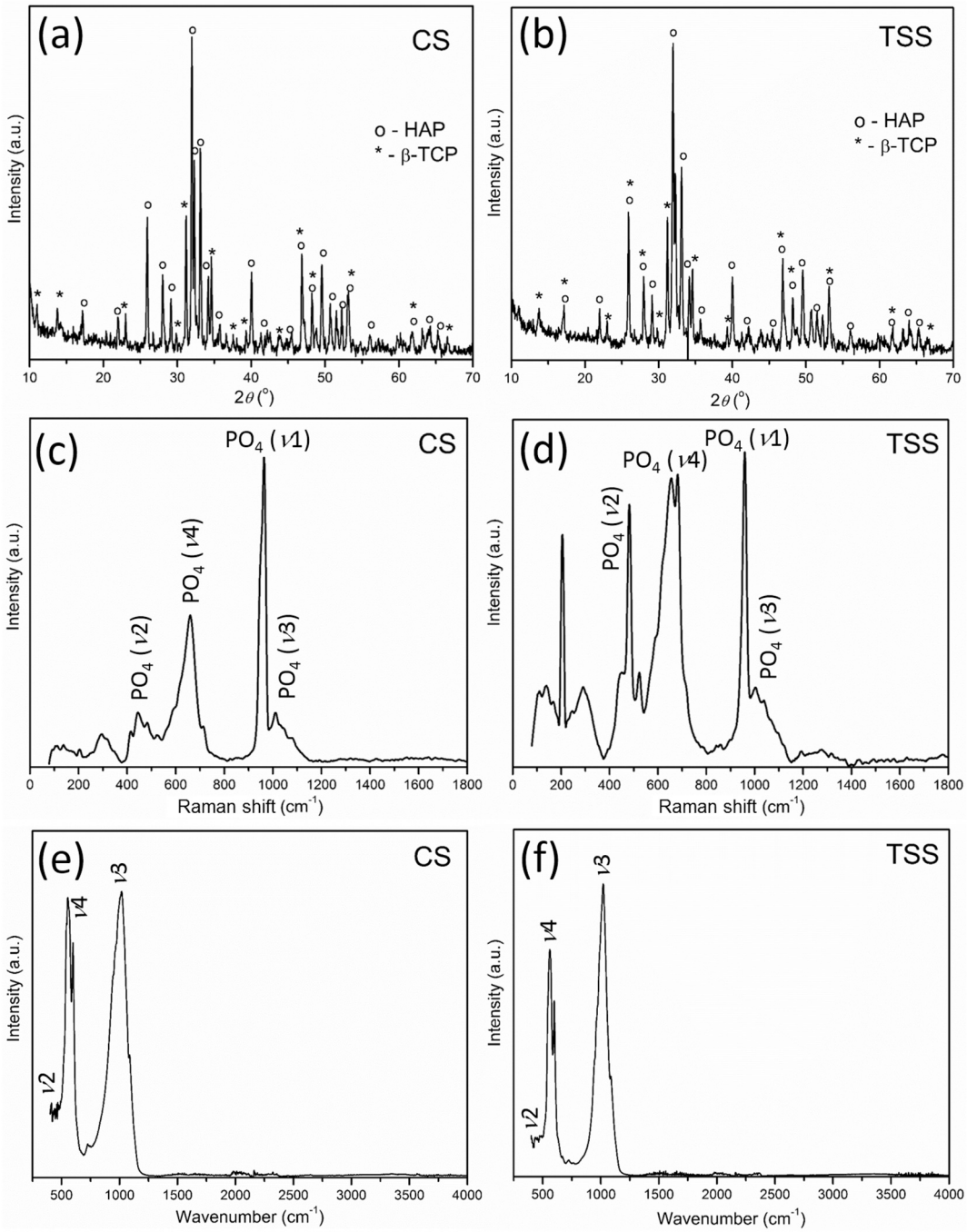

Fig. 4. Sintered pellets: XRD pattern (a) CS, (b) TSS; Raman spectra (c) CS, (d) TSS; FTIR spectra (e) CS, and (f) TSS.

The described characteristics of Co:HAP suggest that the powder can be suitable for sintering.

Before sintering, the thermal stability of the Co:HAP powder was examined. The TG/dTG/DTA curves presented in Fig. 3 show several obvious steps of mass loss and endothermic peaks. The first mass loss of about 1.4 wt% is due to the release of surface water at 100–120 °C, which is accompanied with an endothermic feature on the DTA curve. An additional mass loss of 1 wt%, which occurred upon further heating to 600 °C and was accompanied with a very broad endothermic peak, is attributed to the removal of the lattice water. Further heating, from 600 to 1200 °C, was accompanied with constant dehydroxylation which is observed as a constant mass loss [6]. Dehydroxylation can be accompanied by decomposition, causing partial phase transformation from HAP to β-tricalcium phosphate (β-TCP) and successively to α-tricalcium phosphate (α-TCP) [6]. Total mass loss of 3.9 wt% was measured.

3.2. Characteristics of CS and TSS sintered targets

The analysis of the XRD data collected on the CS and TSS sintered materials, Fig. 4 (a, b) and Table 1, shows that both procedures yield a mixture of two phases, HAP and β-TCP, but the HAP-to-β-TCP percentage ratio, unit cell parameters, average crystallite sizes, and crystallinity are to some extent different. In both cases, the crystallinity of CS and TSS slightly increases (84 and 81%, respectively) compared to the value for the Co:HAP powder (76%). A greater amount of β-TCP in the CS sample than in the TSS one, as well as a higher crystallinity, may be due to a higher sintering temperature which is in this case a more dominant factor than the dwell time. The analysis of Raman spectra, Fig. 4 (c, d),

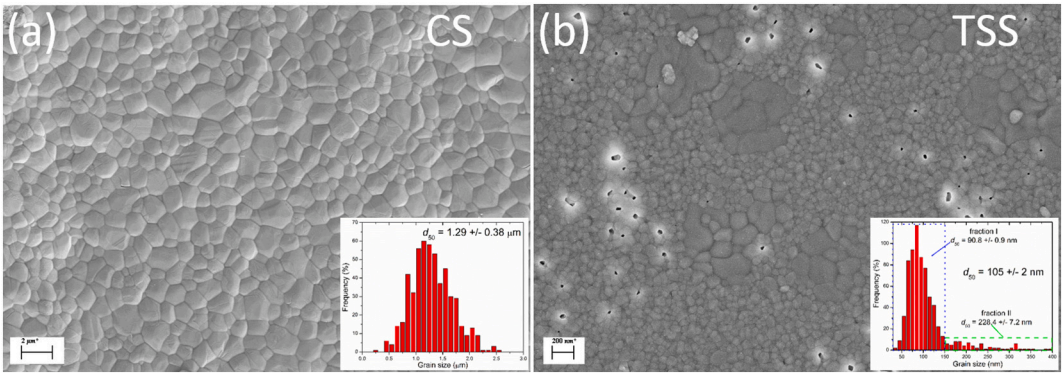

Fig. 5. FESEM images with the inserted grain size distribution of (a) CS, and (b) TSS sintered pellets.

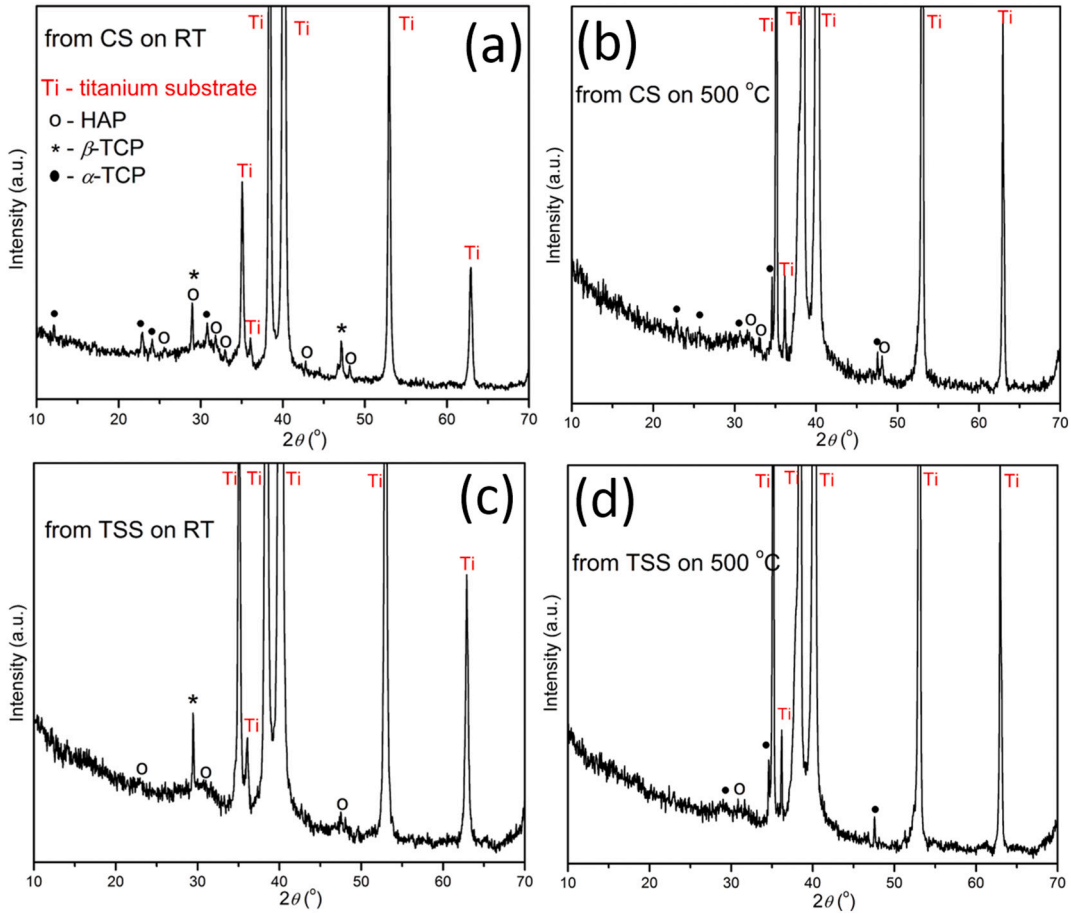

Fig. 6. XRD pattern of the thin films on the Ti substrate: (a) from CS at RT, (b) from CS at 500 °C, (c) from TSS at RT, and (d) from TSS at 500 °C.

reveals the increase of the β-TCP phase. Since β-TCP has no structural OH groups, the FT-IR technique is ideal to study changes on the vibrational bands of the OH group, near 630 and 3570 cm^{-1}, during phase evolution from HAP to β-TCP [22,23]. Hence, the FTIR spectra, Fig. 4 (e, f), reveal a decreases of the relative content of the structural OH groups, confirming the decrease of the HAP content.

It is known that stoichiometric HAP is thermally stable, decomposing to β-TCP at temperatures above 1100 °C [6]. However, it has been found that Co:HAP is less thermally stable and it begins to decompose to TCP at 800 °C [24]. Thus, a relatively large amount of the β-TCP crystal phase in the CS and TSS samples is related to both the amount of cobalt in the HAP crystal structure and the sintering conditions (final temperature and dwell time).

The microstructure of the CS and TSS samples, along with the corresponding histograms of the grain size distribution, is presented in Fig. 5. The CS sample has a fully dense uniform microstructure consisting of grains with an average size about 1.3 μm, Fig. 5 (a). The percentage of open porosity of the TSS sample is less than 1.5%. From Fig. 5 (b) the existence of two different microstructures can be observed, where the majority of grains are smaller than 100 nm, about 90 nm in average; a smaller fraction consists of grains with an average size of about 230 nm.

The study shows that a highly dense (Ca + Co)P target with a significantly different microstructure and a somewhat different HAP-to-β-TCP percentage ratio can be successfully prepared from a nanostructured Co:HAP powder by applying different sintering approaches.

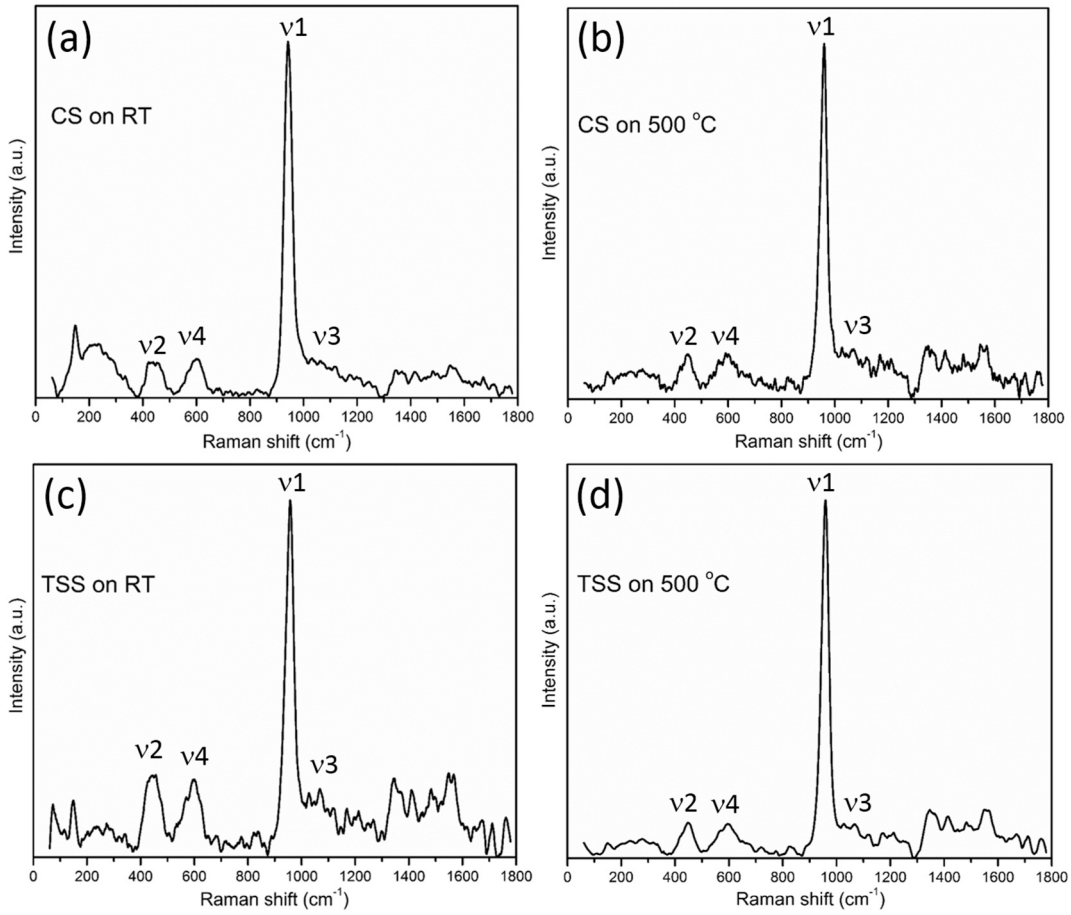

Fig. 7. Raman spectra of the thin films on the Ti substrate: (a) from CS at RT, (b) from CS at 500 °C, (c) from TSS at RT, and (d) from TSS at 500 °C.

3.3. Characteristics of (Ca + Co)P coatings on Ti

The XRD patterns of the coatings deposited on a Ti substrate at different temperatures, using CS and TSS pallets as targets for laser deposition, are shown in Fig. 6. The high-intensity reflections in the XRD patterns can be attributed to the Ti substrate. All the coatings have a crystalline structure with degree of crystallinity between 61 and 67%. The main difference between the coatings lies in their phase composition, Table 1. The coating obtained from the CS target, deposited on a Ti substrate at 25 °C, consisted of HAP, β-TCP and α-TCP. However, when the substrate was heated at 500 °C, we obtained a coating consisted of HAP and α-TCP, suggesting that β-TCP had been completely transformed to α-TCP. The coating obtained using the TSS target, deposited on a Ti substrate at 25 °C, consisted of HAP and β-TCP; when the substrate was heated at 500 °C, the obtained coating consisted of HAP and α-TCP. As far as the α- and β-TCP phases are concerned, the latter one is proved to be biocompatible, while the former one is reported to be cytotoxic [25]. The cytotoxicity of α-TCP is due to its hydrolysis in aqueous media resulting in a decreased pH of the medium due to phosphoric acid, formed during the hydrolysis. Therefore, the coating obtained using the TSS target, deposited on a Ti substrate at 25 °C, consisting of HAP and β-TCP, can be recommended for biomedical implant applications.

The presence of the α-TCP phase in the coatings deposited at 500 °C can be associated with the nanosecond ablation mechanism. The laser ablation of a solid target leads to the generation of a plasma formed by ions, molecules and liquid droplets at a temperature of thousand K. The expanding plasma quickly cools down in few microseconds, depositing on the substrate surface. In this scenario it can be considered that the heated substrate supports the stabilization of the high temperature stable α phase. Furthermore, it has to be considered that, although the transformation from β to α takes place at temperature above 1125 °C, the presence of cobalt as a doping ion can reduce the transition temperature, as it has been observed for some ion-doped TCP [26,27]. These results

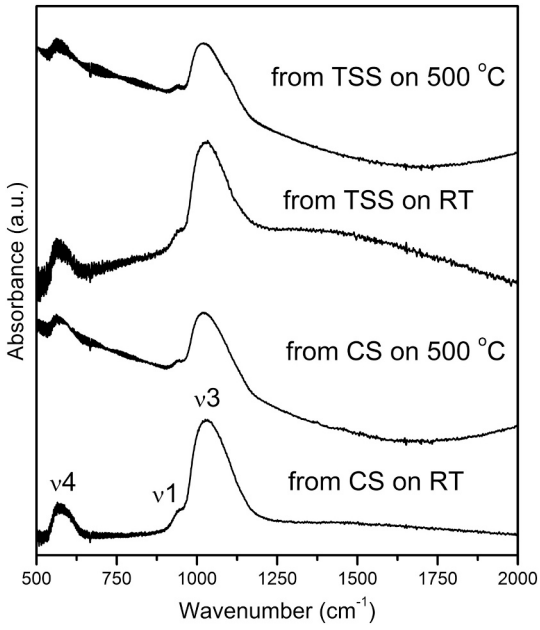

Fig. 8. FTIR spectra of the thin films on the Ti substrate: (a) from CS at RT, (b) from CS at 500 °C, (c) from TSS at RT, and (d) from TSS at 500 °C.

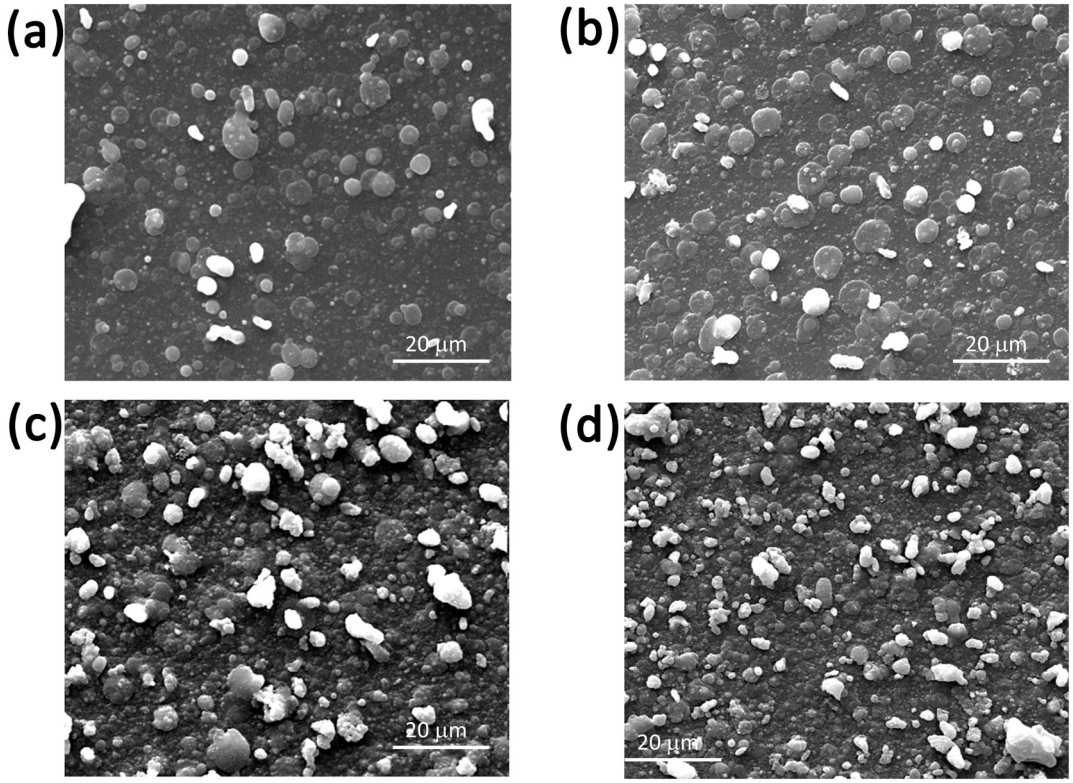

Fig. 9. SEM images of the thin films on the Ti substrate: (a) from TSS at RT, (b) from CS at RT, (c) from TSS at 500 °C, and (d) from CS at 500 °C.

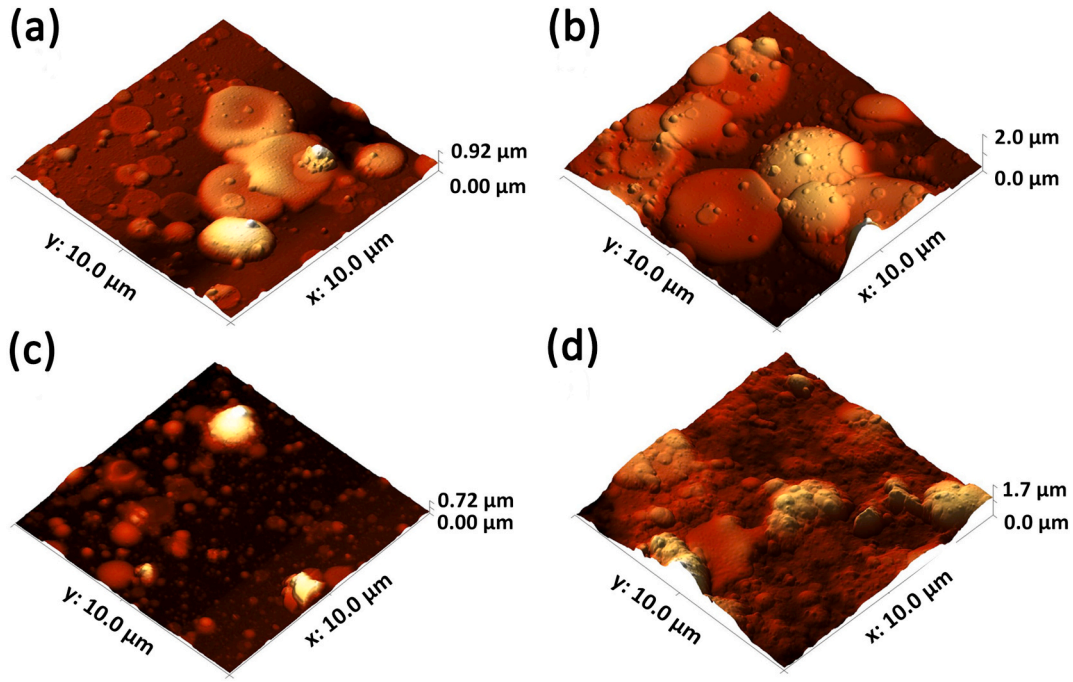

Fig. 10. AFM height signal 3D maps (10 × 10 µm^2 area) of the thin films deposited on the Ti substrate at (a, b) RT and (c, d) 500 °C, from targets obtained through CS (b, d) and TSS (a, c) targets.

show that the phase composition of coatings can be tailored by adjusting the (even slightly different) phase composition of the targets and the temperature of the Ti substrate during deposition.

The Raman spectra of the coatings deposited on the Ti substrate are presented in Fig. 7. The spectra are similar, containing typical vibration modes (ν1, ν2, ν3 and ν4) of PO_4^{3-}. A broad bend between 100 and 400 cm^{-1} can be attributed to TiO_2 which naturally exists on Ti surface as a coating [3]. Actually, TiO_2 in the rutile form exhibits three characteristic Raman bends at 140, 430 and 590 cm^{-1}, which correspond to the symmetries of B_{1g}, E_g and A_{1g}, respectively; while the broad bend centered near 230 cm^{-1} is due to the multiple phonon scattering [28–30]. From Fig. 7, it can be seen that the intensity ratio of PO_4^{3-}

Table 2
Hardness of Co:HAP coatings on Ti substrates deposited from CS and TSS targets at 25 and 500 °C substrate temperature.

Target	Deposition temperature (°C)	Hardness (GPa)
CS	RT	27 ± 3
	500	20 ± 2
TSS	RT	18 ± 4
	500	16 ± 3

vibration modes and the modes attributed to TiO_2 is different for the coatings deposited at 25 and 500 °C. More precisely, the peak intensities of PO_4^{3-} vibration modes are higher for the coatings deposited at 500 °C, while the opposite trend is observed for the TiO_2 bends. Raman analyses confirmed the formation of calcium phosphate phases with a more ordered crystal symmetry when the coatings were deposited at 500 °C. These results are in agreement with the degree of crystallinity calculated from the XRD data, Table 1. The FTIR spectra of the coatings deposited on the Ti substrate at 25 and 500 °C are presented in Fig. 8 indicating a pure CaP phase without impurities on the surface.

The SEM images of CS and TSS films deposited on titanium substrates at different temperatures (RT and 500 °C) show uniform and compact coatings irrespective of the deposition temperature (see Fig. 9). The coatings deposited at RT show round shaped fused micrometric particles coalesced against a background composed of submicrometric ones. Since the mobility of the particles increased at increased deposition temperature, the films deposited at 500 °C were denser and particles became sharp-hedged.

The AFM micrographs of the (Ca + Co)P coatings deposited on Ti at 25 °C (Fig. 10 (a) and (b)) and 500 °C (Fig. 10 (c) and (d)) confirm the uniform coverage of the substrate, regardless of the deposition temperature, although important differences can be highlighted as regards the particles' shape and surface roughness. In particular, the coatings deposited at RT are mainly composed of droplet-shaped particles, frequently overlapping, with diameters in the 1.2–4.7 μm range, along with smaller and flattened circular particles having diameters between 45 nm and roughly 1.3 μm. The RMS roughness values (R_q) for the samples deposited at RT, evaluated using the Gwyddion 2.58 open-source software [31], are 317.4 ± 155.8 nm and 150.3 ± 65.57 nm for the coatings obtained via the CS and TSS sintering routes, respectively. The coatings deposited on a Ti substrate at 500 °C show a different morphology (Fig. 10 (c) and (d) for the TSS and CS routes, respectively); they are mainly composed of finer particles with irregular and sharp edges, as compared to coatings deposited at RT. Round-shaped particles are still detectable only in the sample obtained via the TSS method. Moreover, while the estimated R_q increases up to 413.7 ± 197.4 nm for coatings obtained via the CS route (Fig. 10 (d)), the films obtained by the TSS route show a reduction of the RMS roughness at high temperature, with an estimated value of 104.59 ± 51.57 nm.

The (Ca + Co)P coatings deposited on Ti at the 25 and 500 °C from CS and TSS targets are about 0.3 ± 0.1 μm thick with the hardness ranging from of 16 ± 3 up to and 27 ± 3 GPa (see Table 2). The experimental data on the composite hardness versus the inverse imprint diagonal are presented as graphs in Fig. 11. The main reason for a somewhat lower hardness of the coatings deposited at 500 °C from both targets may be the presence of the α–TCP crystal phase, since α–TCP has inferior mechanical properties, both hardness and fracture toughness, compared to

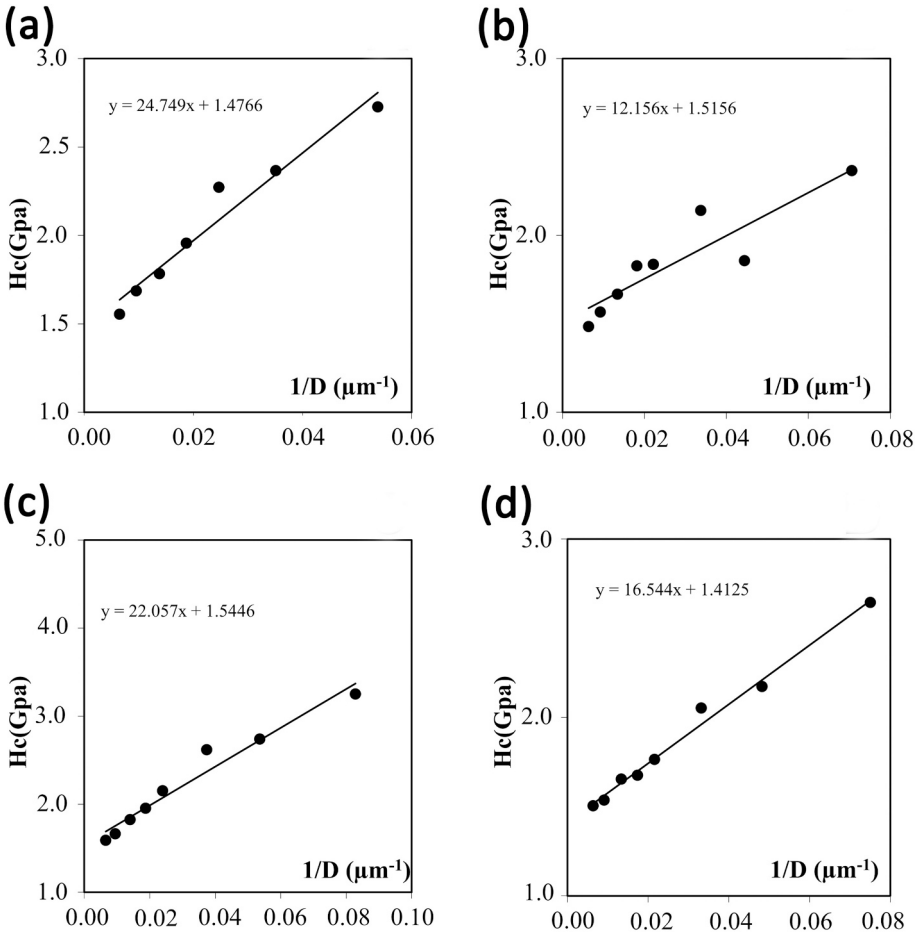

Fig. 11. Composite hardness versus the inverse imprint diagonal for the Co-HA film on the Ti substrate deposited from the CS target at RT (a) and 500 °C (b), and from the TSS target at RT (c), and 500 °C (d).

β–TCP.

4. Conclusion

Two different sintering methods, the conventional and two-step approaches, were applied to a nanostructured Co:HAP powder in order to fabricate calcium phosphate-based targets for coatings deposition by PLD. The results show that in both cases BCP ceramics (targets) were prepared with a slightly different HAP-to-β–TCP amount ratio and significant difference in microstructure. While the CS method yields fully dense ceramics with an average grain size of 1.3 μm, the open porosity of the ceramics prepared by TSS was about 1.5%, with a bimodal grain-size distribution and a predominant grain size below 100 nm.

The 0.3 μm thick (Ca + Co)P coatings were prepared by the PLD of the (Ca + Co)P sintered materials as targets, at two different temperatures of the Ti substrate, 25 and 500 °C. The results of the XRD analysis show that the phase composition of the (Ca + Co)P coatings depends on the phase composition of the targets as well as on the temperature of the Ti substrate. The coating prepared at 25 °C using the CS target consisted of three calcium phosphate phases, HAP, β–TCP and α–TCP, while the coating obtained using the TSS target was biphasic, containing HAP and β–TCP. However, when the substrate was heated at 500 °C, the deposited coatings were composed of HAP and α–TCP regardless of whether the CS or the TSS was used. Furthermore, due to a different phase composition, the (Ca + Co)P coatings deposited at 25 °C showed improved hardness compared to those deposited at 500 °C. The R_q values for the coatings obtained via the CS and TSS sintering routes deposited at RT are 317.4 ± 155.8 nm and 150.3 ± 65.57 nm, respectively. For the coatings deposited at 500 °C via the CS route, the R_q increased up to 413.7 ± 197.4 nm, whereas for those obtained via the TSS route, it showed a reduction down to 104.59 ± 51.57 nm. The obtained results show that the phase composition, morphology and mechanical properties of the (Ca + Co)P coatings on a Ti substrate can be tailored by employing (Ca + Co)P targets with different microstructures, and also by varying the temperature of the Ti substrate during laser deposition. The coating obtained using the TSS target, deposited on a Ti substrate at 25 °C, consisted of HAP and β-TCP, can be recommended for biomedical implant applications.

CRediT authorship contribution statement

Smilja Marković: Conceptualization, Methodology, Writing - Reviewing and Editing, Supervision; **Julietta V. Rau**: Conceptualization, Methodology, Writing - Reviewing and Editing; **Angela De Bonis**: Investigation, Writing - Reviewing and Editing; **Giovanni De Bellis**: Investigation, Writing - Reviewing and Editing; **Zoran Stojanović**: Investigation; **Ljiljana Veselinović**: Investigation; **Miodrag Mitrić**: Investigation; **Nenad Ignjatović**: Investigation; **Srečo Davor Škapin**: Investigation, Writing; **Damjan Vengust**: Investigation.

Declaration of competing interest

The authors declare that they have no known competing financial interests or personal relationships that could have appeared to influence the work reported in this paper.

Acknowledgements

This work was financially supported by the Ministry of Education, Science and Technological Development of Republic of Serbia, through the agreement related to the realization and funding of scientific research work at the Institute of Technical Sciences of SASA in 2022, Contract number: 451-03-68/2022-14/200175. Authors are grateful to Mr. Luca Imperatori for performing the Vickers microhardness measurements. We acknowledge the CENN Nanocenter for the use of Confocal Raman spectrometer NTEGRA Spectra I.

References

[1] J. Van der Stok, E.M.M. Van Lieshout, Y. El-Massoudi, G.H. Van Kralingen, P. Patka, Bone substitutes in the Netherlands—a systematic literature review, Acta Biomater. 7 (2011) 739–750.
[2] S. Marković, L. Veselinović, M.J. Lukić, L. Karanović, I. Bračko, N. Ignjatović, D. Uskoković, Synthetical bone-like and biological hydroxyapatites: a comparative study of crystal structure and morphology, Biomed. Mater. 6 (2011), 045005 (13pp).
[3] K.A. Prosolov, K.S. Popova, O.A. Belyavskaya, J.V. Rau, K.A. Gross, A. Ubelis, Yu. P. Sharkeev, RF magnetron-sputtered coatings deposited from biphasic calcium phosphate targets for biomedical implant applications, Bioact. Mater. 2 (2017) 170–176.
[4] G. Daculsi, R.Z. Legeros, E. Nerry, K. Lynch, B. Kerebel, Transformation of biphasic calcium phosphate ceramics in vivo: ultrastructural and physicochemical characterization, J. Biomed. Mater. Res. 23 (1989) 883–894.
[5] G. Daculsi, O. Laboux, O. Malard, P. Weiss, Current state of the art of biphasic calcium phosphate bioceramics, J. Mater. Sci. Mater. Med. 14 (2003) 195–200.
[6] M. Lukić, Z. Stojanović, S.D. Škapin, M. Maček-Kržmanc, M. Mitrić, S. Marković, D. Uskoković, Dense fine-grained biphasic calcium phosphate (BCP) bioceramics designed by two-step sintering, J. Eur. Ceram. Soc. 31 (2011) 19–27.
[7] M.R. Pantović Pavlović, M.M. Pavlović, S. Eraković, J.S. Stevanović, V.V. Panić, N. Ignjatović, Simultaneous anodization/anaphoretic electrodeposition synthesis of nano calcium phosphate/titanium oxide composite coatings assisted with chitosan oligosaccharide lactate, Mater. Lett. 261 (2020), 127121.
[8] V. Nelea, C. Morosanu, M. Iliescu, I.N. Mihailescu, Microstructure and mechanical properties of hydroxyapatite thin films grown by RF magnetron sputtering, Surf. Coat. Technol. 173 (2003) 315–322.
[9] J.V. Rau, A. Generosi, S. Laureti, V.S. Komlev, D. Ferro, S. Nunziante Cesaro, B. Paci, V. Rossi Albertini, E. Agostinelli, S.M. Barinov, Physico-chemical investigation of pulsed laser deposited carbonated hydroxyapatite films on titanium, ACS Appl. Mater. Interfaces 8 (2009) 1813–1820.
[10] D. Arcos, M. Vallet-Regí, Substituted hydroxyapatite coatings of bone implants, J. Mater. Chem. B 8 (9) (2020) 1781–1800.
[11] K.P. Tank, K.S. Chudasama, V.S. Thaker, M.J. Joshi, Cobalt-doped nanohydroxyapatite: synthesis, characterization, antimicrobial and hemolytic studies, J. Nanopart. Res. 15 (2013) 1644.
[12] N. Ignjatović, Z. Ajduković, J. Rajković, S. Najman, D. Mihailović, D. Uskoković, Enhanced osteogenesis of nanosized cobalt-substituted hydroxyapatite, J. Bionic Eng. 12 (2015) 604–612.
[13] R. Drevet, Y. Zhukova, S. Dubinskiy, A. Kazakbiev, V. Naumenko, M. Abakumov, J. Fauré, H. Benhayoune, S. Prokoshkin, Electrodeposition of cobalt-substituted calcium phosphate coatings on Ti22Nb6Zr alloy for bone implant applications, J. Alloys Compd. 793 (2019) 576–582.
[14] M.J. Lukić, S.D. Škapin, S. Marković, D. Uskoković, Processing route to full dense nanostructured HAp bioceramics: from powder synthesis to sintering, J. Am. Ceram. Soc. 95 (2012) 3394–3402.
[15] Z. Stojanović, L. Veselinović, S. Marković, N. Ignjatović, D. Uskoković, Hydrothermal synthesis of nanosized pure and cobalt-exchanged hydroxyapatite, Mater. Manuf. Process. 24 (10) (2009) 1096–1103.
[16] L. Veselinović, L. Karanović, Z. Stojanović, I. Bračko, S. Marković, N. Ignjatović, D. Uskoković, Crystal structure of cobalt-substituted calcium hydroxyapatite nanopowders prepared by hydrothermal processing, J. Appl. Crystallogr. 43 (2010) 320–327.
[17] N. Ignjatović, Z. Ajduković, V. Savić, S. Najman, D. Mihailović, P. Vasiljević, Z. Stojanović, V. Uskoković, D. Uskoković, Nanoparticles of cobalt-substituted hydroxyapatite in regeneration of mandibular osteoporotic bones, J. Mater. Sci. Mater. Med. 24 (2013) 343–354.
[18] Z.R. Ajduković, T.M. Mihajilov-Krstev, N.L. Ignjatović, Z. Stojanović, S. B. Mladenović-Antić, B.D. Kocić, S. Najman, N.D. Petrović, D.P. Uskoković, In vitro evaluation of nanoscale hydroxyapatite-based bone reconstructive materials with antimicrobial properties, J. Nanosci. Nanotechnol. 16 (2016) 1420–1428.
[19] H.P. Klug, L.E. Alexander, X-ray Diffraction Procedures for Polycrystalline and Amorphous Materials, 4th edn, Wiley, New York, 1954.
[20] B. Joensson, S. Hogmark, Hardness measurements of thin films, Thin Solid Films 114 (1984) 257–269.
[21] D. Ferro, J.V. Rau, V. Rossi Albertini, A. Generosi, R. Teghil, S.M. Barinov, Pulsed laser deposited hard TiC, ZrC, HfC and TaC films on titanium: hardness and an energy-dispersive X-ray diffraction study, Surf. Coat. Technol. 202 (2008) 1455–1461.
[22] A. Siddharthan, T.S.Sampath Kumar, S.K. Seshadri, Synthesis andcharacterization of nanocrystalline apatites from eggshells at different Ca/P ratios, Biomed. Mater. 4 (2009), 045010 (9pp).
[23] S. Marković, M.J. Lukić, S.D. Škapin, B. Stojanović, D. Uskoković, Designing, fabrication and characterization of nanostructured functionally graded HAp/BCP ceramics, Ceram. Inter. 41 (2015) 2654–2667.
[24] E. Kramer, M. Conklin, M. Zilm, E. Itzkowitz, M. Wei, A comparative study of the sintering and cell behavior of pure and cobalt substituted hydroxyapatite, Bioceram. Dev. Appl. 4 (1) (2014), 1000077 (8 pp.).
[25] M. Tamai, N. Ryusuke, T. Toshie, Cytotoxicity of various calcium phosphate ceramics, Key Eng. Mater. 309–311 (2006) 263–266.
[26] S.V. Dorozhkin, Calcium orthophosphates, J. Mater. Sci. 42 (2007) 1061–1095.
[27] J.W. Reid, A. Pietak, M. Sayer, D. Dunfield, T.J.N. Smith, Phase formation and evolution in the silicon substituted tricalcium phosphate/apatite system, Biomaterials 26 (2005) 2887–2897.

[28] V. Tamilselvan, D. Yuvaraj, R.R. Kumar, K.N. Rao, Growth of rutile TiO2 nanorods on TiO2 seed layer deposited by electron beam evaporation, Appl. Surf. Sci. 258 (2012) 4283–4287.
[29] H.L. Ma, J.Y. Yang, Y. Dai, Y.B. Zhang, B. Lu, G.H. Ma, Raman study of phase transformation of TiO2 rutile single crystal irradiated by infrared femtosecond laser, Appl. Surf. Sci. 253 (2007) 7497–7500.
[30] S. Challagulla, K. Tarafder, R. Ganesan, S. Roy, Structure sensitive photocatalytic reduction of nitroarenes over TiO2, Sci. Rep. 7 (2017) 8783.
[31] D. Nečas, P. Klapetek, Gwyddion: an open-source software for SPM data analysis, Cent. Eur. J. Phys. 10 (1) (2012) 181–188.